



# Structural properties, Judd–Ofelt calculations, and near infrared to visible photon up-conversion in $\text{Er}^{3+}/\text{Yb}^{3+}$ doped $\text{BaTiO}_3$ phosphors under excitation at 1500 nm

M. Vega,<sup>\*ab</sup> P. Alemany,<sup>c</sup> I. R. Martin<sup>d</sup> and J. Llanos<sup>\*b</sup>

The structural and up-conversion properties of  $\text{BaTiO}_3$  phosphors doped with  $\text{Er}^{3+}/\text{Yb}^{3+}$  have been studied. All phases were synthesized using the sol–gel process and characterized by X-ray powder diffraction (PXRD), Raman spectroscopy, optical absorption spectroscopy (Judd–Ofelt theory), and scanning electron microscopy (SEM). Photoluminescence (PL) and time-resolved luminescence measures were employed to monitor the photon upconversion (UC) process in the synthesized phosphors. The results of PXRD show that all synthesized phases crystallize in a perovskite structure, where rare earth ions replace both  $\text{Ba}^{2+}$  and  $\text{Ti}^{4+}$  cations. Raman spectra confirm the coexistence of both cubic and tetragonal phases. Photon UC was studied under excitation at 1500 nm. The emission spectrum shows a strong emission at 975 nm ( $^4\text{I}_{11/2} \rightarrow ^4\text{I}_{15/2}$ ) and a weak emission at 660 nm ( $^4\text{F}_{9/2} \rightarrow ^4\text{I}_{15/2}$ ). To unravel the mechanism of photon UC, the dependence of the emission intensity on the pump power of the incident laser was also measured. Furthermore, the decay curves for the 975 nm emission upon excitation at 1500 and 800 nm were also recorded. These results of our study point towards a GSA/ESA type mechanism for photon UC in this material.

Received 26th December 2016  
Accepted 1st February 2017

DOI: 10.1039/c6ra28725e  
[rsc.li/rsc-advances](http://rsc.li/rsc-advances)

## 1. Introduction

The conversion of sunlight directly into electricity using photovoltaic devices is one of the most attractive options for renewable energy generation, mainly due to the zero emission of polluting gases as well as the permanent resource availability over wide geographical areas. Most of the commercial solar panels use semiconductor materials such as silicon and their efficiency is largely determined by the magnitude of the band gap.<sup>1</sup> The overall efficiency is, however, limited by many different factors, including among them spectral losses. Although photons with energies above the band gap are also absorbed, they relax the excess energy as heat (thermalization). On the other hand, photons with energies below the band gap are not absorbed at all and do not contribute to the generation of electricity (transmission).<sup>1,2</sup> For this reason, photon conversion arises as an attractive option to reduce spectral losses and increase the efficiency of solar cells.<sup>3–6</sup> Among photon

conversion phenomena, upconversion (UC) can transform photons from the infrared region of the solar spectrum into photons in the visible region, a process that may increase the efficiency of solar energy harvesting by reducing transmission losses.<sup>3–7</sup>

UC consists in the successive absorption of two or more long wavelength (IR) photons and the subsequent emission of a photon with a shorter wavelength (Vis).<sup>8,9</sup> The conversion process requires the participation of a luminescent material having multiple energy levels with the appropriate energy spacing. In this respect, lanthanide ions offer interesting features for UC materials, since the energy levels within the 4f shell range from the near infrared to the ultraviolet part of the electromagnetic spectrum. Among lanthanide ions,  $\text{Pr}^{3+}$ ,  $\text{Nd}^{3+}$ ,  $\text{Dy}^{3+}$ ,  $\text{Ho}^{3+}$ ,  $\text{Er}^{3+}$  and  $\text{Tm}^{3+}$  have been investigated as activators for upconversion materials in solar cells.<sup>10,11</sup>

In optical materials doped with one single type of activator ion, one of the important parameters affecting the UC process is the absorption cross section of the rare earth ions. Since many activator ions exhibit low absorption, upconverting materials doped with just one type of activator ion, show relatively low efficiencies.<sup>7,8,12</sup> To increase the overall efficiency of the UC process, sensitizer ions with sufficient absorption in the infrared region, are often included as co-dopants. Due to its range of absorption in the near infrared region (900–1100 nm) corresponding to the  $^2\text{F}_{5/2}–^2\text{F}_{7/2}$  transition,  $\text{Yb}^{3+}$  is usually used

<sup>a</sup>Departamento de Química, Facultad de Ciencias, Universidad de Chile, Casilla 635, Santiago, Chile. E-mail: [mvega02@ucn.cl](mailto:mvega02@ucn.cl); Tel: +56 55 235 5606

<sup>b</sup>Departamento de Química, Universidad Católica del Norte, Avda. Angamos 0610, Antofagasta, Chile. E-mail: [jllanos@ucn.cl](mailto:jllanos@ucn.cl)

<sup>c</sup>Departament de Ciència de Materials i Química Física, Institut de Química Teòrica i Computacional (IQTCUB), Universitat de Barcelona, 08028 Barcelona, Spain

<sup>d</sup>Departamento de Física, Instituto de Materiales y Nanotecnología (IMN), Universidad de La Laguna, 38206 La Laguna, Tenerife, Spain



as a sensitizer ion. Furthermore, the  $^2F_{5/2}-^2F_{7/2}$  transition for  $Yb^{3+}$  coincides with f-f transitions of several lanthanide ions ( $Er^{3+}$ ,  $Tm^{3+}$  and  $Ho^{3+}$ ) used in UC materials, facilitating an efficient energy transfer from the sensitizer  $Yb^{3+}$  ions to the activator ions.<sup>10,12</sup>

On the other hand, fluorides due to their low phonon energies<sup>9,13</sup> have been found to be among the most efficient matrices for UC materials. However, due to toxicity problems and their poor chemical, thermal and mechanical stability, application of fluorides in technological devices has had a limited success.<sup>14</sup> In comparison with fluorides, oxides exhibit larger phonon energies, but excellent chemical, thermal and mechanical stabilities. An interesting oxide in this respect is barium titanate ( $BaTiO_3$ ). Its relatively low phonon energy (around  $700\text{ cm}^{-1}$ ) together with a good insulating behavior and excellent physical and chemical stabilities make it an excellent candidate for the development of new upconversion phosphors.<sup>15</sup>

In all these systems,  $Ln^{3+}$  ions due to their ionic size are expected to occupy the  $A^{2+}$  sites in the  $ABO_3$  lattice and, therefore, the excess positive charge must be compensated. However, it is also possible to replace some of the  $B^{4+}$  ions by  $Ln^{3+}$ , keeping the overall charge neutrality. In a previous paper<sup>16</sup> we reported on the effects of  $Eu^{3+}$  substitution on the luminescent and magnetic properties of  $BaTiO_3$ . We observed that at low concentrations the rare earth cations replace the  $Ti^{4+}$  sites, whereas both sites,  $Ba^{2+}$  and  $Ti^{4+}$ , are replaced when the concentration of lanthanide cations is increased.

In the present paper, we report on the synthesis of  $BaTiO_3$  based phosphor, codoped with  $Er^{3+}$  and  $Yb^{3+}$  via the sol-gel process and the measurement of its IR to visible up-conversion luminescent properties recorded under a 1500 nm excitation.

## 2. Experimental

### 2.1. Synthesis

Parent reagents, tetrabutyl titanate (TBT) (97%), erbium nitrate (99.9%), ytterbium nitrate (99.9%), and barium acetate ( $\geq 99\%$ ) were purchased from Aldrich Chemical Co. and used as received. In a typical procedure, a solution of the stoichiometric amount of  $Ba(CH_3COO)_2$  in 20 mL of acetic acid was aggregated drop-wise to a solution of 2 mL of TBT diluted using 8 mL of acetylacetone. This mixture was heated to 323 K on a hot plate for 2 h under continuous stirring to form the titania sol. Following this, a solution of the respective amounts of  $Er(NO_3)_3 \cdot 5H_2O$  and  $Yb(NO_3)_3 \cdot 5H_2O$  in 5 mL of deionized water were added to the titania sol and heated to 373 K on a hot plate for 24 h to form a brown powder corresponding to the dry barium erbium-ytterbium titanate. Finally, the product obtained was ground in an agate mortar, placed in an alumina boat and annealed for 2 h at 1273 K in a muffle furnace. All synthetic processes were carried out in air.

### 2.2. Characterization

To check the phase purity, powder X-ray diffraction (PXRD) data were collected using a Bruker D8 Advance diffractometer fitted with a graphite monochromator using  $CuK\alpha$  radiation ( $\lambda =$

$1.54057\text{ \AA}$ ) in the range  $10^\circ \leq 2\theta \leq 60^\circ$ , operated at 40 kV and 30 mA. Raman spectra were collected using a Renishaw research Ramanscope 1000 spectrometer equipped with a Peltier-cooled CCD detector and with Leica microscopes. An excitation line of 785 nm was used and did not reveal any significant dispersion. SEM images were obtained using a TESCAN VEGA 3 microscope.

The optical absorption spectrum was measured by using a Agilent Cary 5000 UV-Vis-NIR spectrophotometer. The samples were compressed in order to prepare pellets with a diameter of 6 mm and a thickness about 0.24 mm.

Upconversion spectra were recorded by exciting samples using a commercial 1500 nm laser (Alcatel 1933 SMG) with a maximum power of 80 mW. The laser was focused on the samples using a lens with a 30 mm focal length. The emitted light was focused on the entrance slit of a CCD spectrograph (Andor Shamrock 303i) using a lens with a focal length of 50 mm.

Luminescence decay curves were obtained by exciting samples using a 10 ns pulsed optical parametric oscillator laser (EKSPOLA/NT342/3/UVE). The emission was focused on the entrance of a spectrograph coupled to a photomultiplier (R928 Hamamatsu in the Vis range or 5509-73 Hamamatsu for the NIR range) connected to a digital storage oscilloscope (Tektronix 2430).

## 3. Results and discussion

### 3.1. X-Ray diffraction

The powder diffraction patterns contain sharp and well-defined peaks, indicating good crystallinity for all samples. However, minor shifts in the peak positions were observed when the  $Er^{3+}$  and  $Yb^{3+}$  cations were incorporated into the host  $BaTiO_3$  matrix. Comparing the  $d$ -values with the standard patterns (JCPDS 075-0462),<sup>17</sup> all reflections in the diffractograms can be indexed in the cubic perovskite-type structure of  $BaTiO_3$ , as shown in Fig. 1. As the concentration of dopant ions increases, the crystal structure is maintained. However, at high dopant concentrations ( $BaTiO_3:Er^{3+} 9\%-Yb^{3+} 10\%$ ) the appearance of minority phases related to either precursor materials ( $BaCO_3$ ) or a secondary phase ( $Er_2Ti_2O_7$ ) can be observed.

Incorporation of  $Ln^{3+}$  ions in the structure can occur in both cationic sites ( $Ba^{2+}$  and  $Ti^{4+}$ ), depending on the ionic radius of the rare earth. Tsur *et al.*<sup>18</sup> have reported that for  $BaTiO_3$ ,  $Ba^{2+}$  ions are being replaced by ions with ionic radii  $\geq 0.94\text{ \AA}$ , whereas the  $Ti^{4+}$  ions are being replaced by rare earth ions with ionic radius  $\leq 0.87\text{ \AA}$ . Meanwhile, ions with ionic radii in the range between these values can replace both sites. The ionic radii of  $Ba^{2+}$  and  $Ti^{4+}$  are 1.42 and 0.61  $\text{\AA}$ , respectively, while those of  $Er^{3+}$  and  $Yb^{3+}$  are 0.89 and 0.87  $\text{\AA}$ , respectively.<sup>19</sup> Therefore, according to Tsur *et al.* the  $Er^{3+}$  cation should be able to replace both sites indistinctly, while  $Yb^{3+}$  ions would replace only the  $Ti^{4+}$  ones.<sup>18</sup>

The effect of substitution on the cell volume can be seen in Fig. 2. In general, one can observe that, at low concentrations of both dopants, the cell volume does not show a systematic variation. This is due to random distribution of  $Er^{3+}$  ions in the

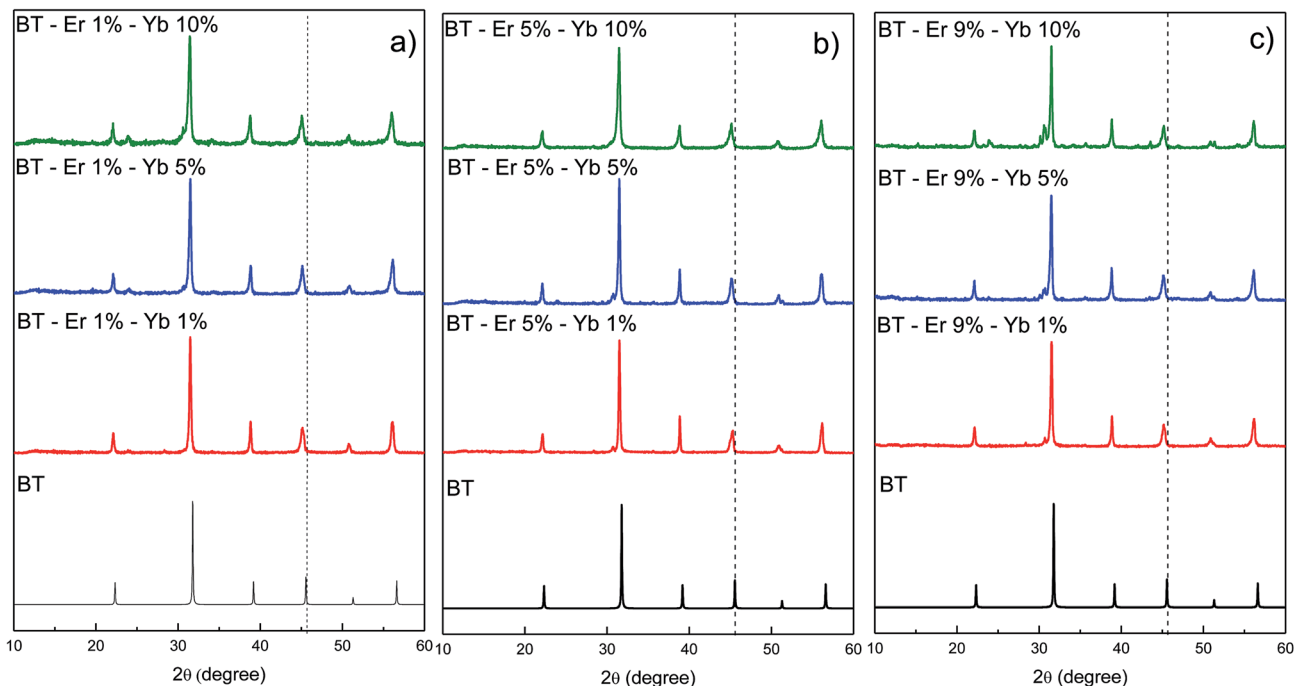


Fig. 1 XRD patterns of the  $\text{BaTiO}_3$  doped with different contents of  $\text{Er}^{3+}$  and  $\text{Yb}^{3+}$  ions.

cationic sites. Moreover, at high concentrations of both dopants a progressive decrease in unit cell volume is observed. Since the  $\text{Yb}^{3+}$  ions only replace  $\text{Ti}^{4+}$  ions, at high concentrations of  $\text{Yb}^{3+}$  these sites are mostly occupied. For this reason, as the  $\text{Er}^{3+}$  ion concentration increases in codoped samples, these ions occupy mostly  $\text{Ba}^{2+}$  sites, causing a steady decline in the volume of the unit cell. The values of lattice constants and volume of the unit cell for various dopings are summarized in Table 1.

### 3.2. Raman spectroscopy

While XRD shows only the presence of the cubic phase, it is known that in  $\text{BaTiO}_3$  cubic and tetragonal perovskite phases

may coexist.<sup>20</sup> A way of confirming the presence of the tetragonal phase is to visualize small differences in the local symmetry of the crystal lattice. In the cubic phase  $\text{Ti}^{4+}$  ions occupy the center of octahedra formed by six neighboring  $\text{O}^{2-}$  ions, resulting in a local  $O_h$  symmetry. In the tetragonal phase, one of these  $\text{O}^{2-}$  ions is, however, slightly displaced in the direction of the  $c$  axis, resulting in a local  $C_{4v}$  symmetry, a difference that can be easily monitored by means of Raman spectroscopy.

Raman spectra for three different samples of  $\text{BaTiO}_3:\text{Er}^{3+}/\text{Yb}^{3+}$  phosphors with varying contents in  $\text{Er}^{3+}/\text{Yb}^{3+}$  ions are shown in Fig. 3. In them, the five characteristic bands of the  $\text{BaTiO}_3$  phase, which have been widely reported in literature,<sup>20–26</sup> can be observed: a sharp peak at  $304\text{ cm}^{-1}$  [B1, E (TO + LO)] and broad bands at about  $181\text{ cm}^{-1}$  [A<sub>1</sub> (TO), E (LO)],  $255\text{ cm}^{-1}$  [A<sub>1</sub> (TO<sub>2</sub>)],  $515\text{ cm}^{-1}$  [A<sub>1</sub>, E (TO)], and  $719\text{ cm}^{-1}$  [A<sub>1</sub>, E (LO)]. The sharpness of the peak around  $304\text{ cm}^{-1}$ , which is characteristic of the tetragonal  $\text{BaTiO}_3$  phase, is reduced and becomes indistinct when the tetragonal phase is not dominant.<sup>25</sup> As it

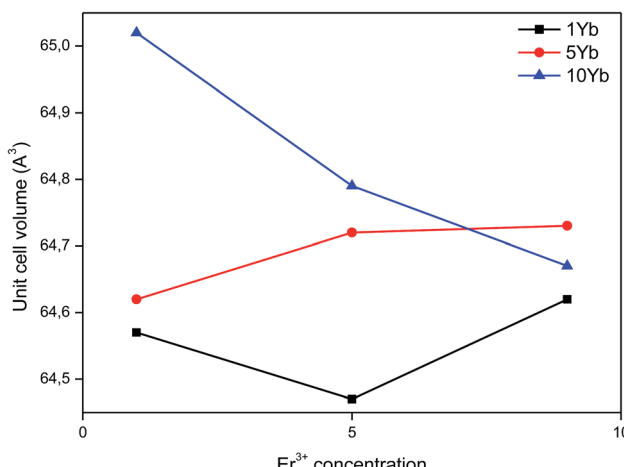


Fig. 2 Variation of the unit-cell volume as a function of the  $\text{Er}^{3+}$  and  $\text{Yb}^{3+}$  contents.

Table 1 Calculated cell parameters of  $\text{BaTiO}_3:\text{Er}^{3+}-\text{Yb}^{3+}$

Sample	$a$ (Å)	$V$ (Å <sup>3</sup> )
$\text{BaTiO}_3:\text{Er}^{3+} 1\%-\text{Yb}^{3+} 1\%$	4.012(9)	64.57
$\text{BaTiO}_3:\text{Er}^{3+} 1\%-\text{Yb}^{3+} 5\%$	4.013(8)	64.62
$\text{BaTiO}_3:\text{Er}^{3+} 1\%-\text{Yb}^{3+} 10\%$	4.021(7)	65.02
$\text{BaTiO}_3:\text{Er}^{3+} 5\%-\text{Yb}^{3+} 1\%$	4.009(12)	64.47
$\text{BaTiO}_3:\text{Er}^{3+} 5\%-\text{Yb}^{3+} 5\%$	4.015(5)	64.72
$\text{BaTiO}_3:\text{Er}^{3+} 5\%-\text{Yb}^{3+} 10\%$	4.016(9)	64.78
$\text{BaTiO}_3:\text{Er}^{3+} 9\%-\text{Yb}^{3+} 1\%$	4.013(1)	64.62
$\text{BaTiO}_3:\text{Er}^{3+} 9\%-\text{Yb}^{3+} 5\%$	4.015(9)	64.73
$\text{BaTiO}_3:\text{Er}^{3+} 9\%-\text{Yb}^{3+} 10\%$	4.014(4)	64.67



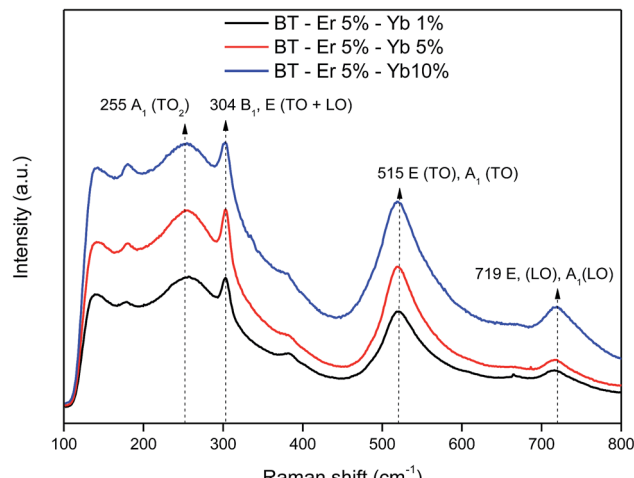


Fig. 3 Raman spectra for bare  $\text{BaTiO}_3$  and  $\text{BaTiO}_3$  doped with different concentrations of  $\text{Er}^{3+}$  and  $\text{Yb}^{3+}$  ions.

can be seen in Fig. 3, this is, however, not the case in our samples, confirming the presence of the tetragonal case. In the recorded spectra, the bands at  $255$  and  $515\text{ cm}^{-1}$  did not show significant changes, while the intensity of those at  $181$ ,  $304$ , and  $719\text{ cm}^{-1}$  increases clearly with the concentration of dopant ions. The band at  $718\text{ cm}^{-1}$ , which can be ascribed to the presence of defects in the  $\text{BaTiO}_3$  lattice is clearly indicative that the formation of the tetragonal phase improves by incorporation of the rare earth cations into the host structure.<sup>23</sup> The observed changes in the Raman spectra corroborate thus the coexistence of both, the cubic and tetragonal phases in the analyzed samples.

### 3.3. Scanning electronic microscopy

SEM images for  $\text{BaTiO}_3:\text{Er}^{3+}$  5%– $\text{Yb}^{3+}$  1% are shown in Fig. 4. The image on the left was generated by secondary electrons (SE) while that on the right by backscattering electrons (BSE). The formation of agglomerates of micron size without a defined

morphology is mainly appreciated in these figures. It is also possible to observe the presence of smaller particles both between grains and on the surface of these. From the BSE image it can be deduced that the sample is homogeneous in composition, which was corroborated by energy dispersive X-ray (EDX) analysis. No large morphological changes between samples as the concentration of the dopant ions is varied were observed.

### 3.4. Optical absorption and Judd–Ofelt analysis

Judd–Ofelt (JO) theory to describe the intensity of f-f transitions in rare-earth ions<sup>27,28</sup> has become a centerpiece of rare-earth spectroscopy and nowadays it is being considered a fundamental stage in the characterization of luminescent materials.<sup>29–31</sup> The great appeal of JO theory is that it allows the prediction oscillator strengths in absorption and luminescence, luminescence branching ratios, and excited-state radiative lifetimes just by using only three empirical parameters,  $\Omega_{(\lambda)}$  ( $\lambda = 2$ ,  $4$ ,  $6$ ), that may be easily determined by fitting calculated intensities to those obtained from an absorption spectrum with known absolute absorption cross sections.<sup>31</sup> Unfortunately the application of JO theory to powder samples is not straightforward and for this reason, quantitative studies for micro- or nanostructured optical materials in the literature are still scarce. To solve these inconveniences an alternative method based on the use of relative optical absorption spectra and the subsequent calibration of oscillator strengths through the use of a radiative lifetime has been devised.<sup>32–34</sup>

From the theoretical point of view, the oscillator strength  $f_{\text{cal}}$  associated to an f-f optical transition is given by

$$f_{\text{cal}}(J \rightarrow J') = \frac{8\pi^2 mc}{3h\lambda_m(2J+1)n^2} \left\{ \frac{n(n^2+2)^2}{9} S_{\text{ed}} + n^3 S_{\text{md}} \right\} \quad (1)$$

where  $J$  and  $J'$  indicate the initial and final manifolds,  $m$  is the electron mass,  $c$  the speed of light,  $h$  Planck's constant,  $\lambda_m$  the barycenter wavelength for the  $J \rightarrow J'$  absorption band,  $n$  the refractive index at  $\lambda_m$  and  $S_{\text{ed}}$  and  $S_{\text{md}}$  are the so-called the electric-dipole and magnetic-dipole line strengths, respectively.

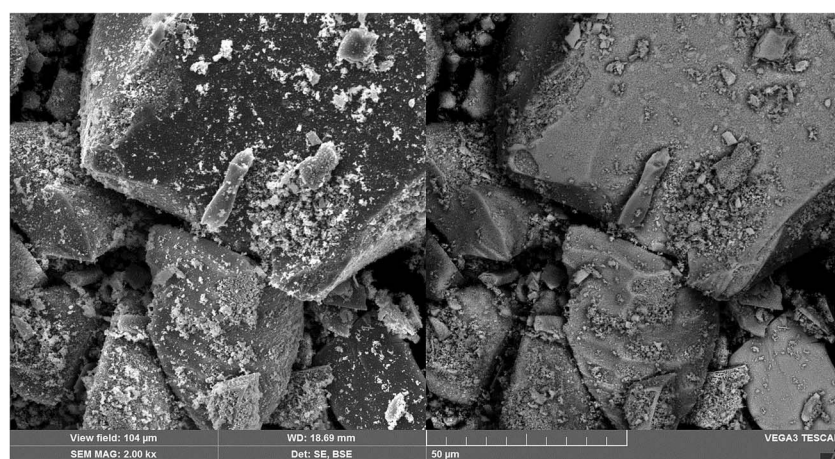


Fig. 4 SEM micrography for a  $\text{BaTiO}_3:\text{Er}^{3+}$  5%– $\text{Yb}^{3+}$  1% sample. Right: Backscattering and Left: secondary electrons.



In the JO theory the electric-dipole line strength  $S_{\text{ed}}$  is expressed in terms of the three JO intensity parameters  $\mathcal{Q}_\lambda$  ( $\lambda = 2, 4, 6$ ):

$$S_{\text{ed}}(J \rightarrow J') = \sum_{\lambda=2,4,6} \mathcal{Q}_\lambda |\langle f^N[SL]J | U^{(\lambda)} | f^N[S'L]J' \rangle|^2 \quad (2)$$

where the terms in brackets are doubly reduced matrix elements for intermediate coupling that have been tabulated in the literature for specific cases, but because in f-f transitions in rare-earth ions the electric dipole transitions arise from a small crystal field perturbation, the matrix elements are not highly dependent on the host material and the matrix elements calculated by Carnall *et al.*<sup>35</sup> for trivalent lanthanides in aqueous solution or  $\text{LaF}_3$  are often used in a JO analysis.

Most of the intensities of  $4f^N$ - $4f^N$  optical transitions have electric-dipole character, although some of them also present magnetic dipole character. For these,  $S_{\text{md}}$  can be expressed in terms of the intermediate coupling coefficients associated to the  $f^N[SL]J$  and  $f^N[S'L]J'$  states as well as the matrix elements of the  $(L + 2S)$  operator between these states and  $S_{\text{md}}$  can be thus readily calculated, using for instance, the RELIC program<sup>31</sup> or using tabulated values calculated for the same transition in other host matrices.

In a standard JO analysis the three intensity parameters  $\mathcal{Q}_\lambda$  ( $\lambda = 2, 4, 6$ ) are being determined by fitting the experimental oscillator strengths  $f_{\text{exp}}$  to the calculated ones,  $f_{\text{calc}}$ , where the experimental oscillator strengths have been extracted from an optical absorption spectrum using

$$f_{\text{exp}}(J \rightarrow J') = \frac{2mc}{\alpha_f h N_T \lambda_m^2} \int_{\text{band}} \alpha(\lambda) d\lambda \quad (3)$$

where  $\alpha_f$  is the fine-structure constant,  $N_T$  the concentration of emitting ions and  $\alpha(\lambda) = 2.3 \times \text{O.D.}/d$  represents the absorption coefficient at wavelength  $\lambda$ , where  $d$  is the sample thickness and O.D. the corresponding optical density.

Besides general problems related to the determination of oscillator strengths from optical absorption spectra (base line corrections, separation of overlapping bands, determination of the band barycenters, *etc.*) when trying to apply the standard procedure to powder samples one encounters the problems that both the active ion concentration and sample thickness are not straightforward quantities to be quantified accurately. An alternative procedure,<sup>34</sup> that has also been employed to perform a JO analysis using absorbances derived from a diffuse reflection spectrum<sup>33</sup> is to follow a two step procedure, performing first a relative JO analysis using the absorption spectrum in terms of optical densities and in a second step, to calibrate the relative JO intensity parameters by using the measured lifetime for a pure radiative transition.

In this procedure, the relative purely electric-dipole line strength

$$S_{\text{ed}}^{\text{rel}}(J \rightarrow J') = \frac{9n}{(n^2 + 2)^2} \frac{C_{\text{JO}}}{\lambda_m} \int_{\text{band}} \text{O.D.}(\lambda) d\lambda \quad (4)$$

is first obtained from the measured absorption spectrum, where  $C_{\text{JO}}$  is a proportionality coefficient relating the relative and absolute line strength values. Fitting of these  $S_{\text{ed}}^{\text{rel}}(J \rightarrow J')$  values to eqn (2) yields then a set of relative JO intensity parameters,  $\mathcal{Q}_\lambda^{\text{rel}}$ , which are proportional to the absolute ones

$$\mathcal{Q}_\lambda = C_{\text{JO}} \mathcal{Q}_\lambda^{\text{rel}} \quad (5)$$

The proportionality constant  $C_{\text{JO}}$  is afterwards determined through the comparison of the calculated and measured lifetimes of a selected predominantly radiative transition. For such a transition, the total transition probability, which is inversely proportional to the lifetime is given by

$$A_T = A_{\text{ed}} + A_{\text{md}} = \tau_{\text{rad}}^{-1} \approx \tau_{\text{exp}}^{-1} \quad (6)$$

where the electric dipole component  $A_{\text{ed}}$  is related to the corresponding line strength by

$$A_{\text{ed}}(J' \rightarrow J) = \frac{64\pi^4 e^2}{3h\lambda_m^3(2J+1)} \frac{n(n^2+2)^2}{9} S_{\text{ed}}(J \rightarrow J') \quad (7)$$

where  $e$  is the electron charge.

To determine the proportionality constant  $C_{\text{JO}}$  one has thus to subtract first the magnetic dipole contribution (calculated using data tabulated in ref. 36) from the total transition probability to obtain the electric dipole probability. Then  $C_{\text{JO}}$  can be simply obtained by combining eqn (2) and (5).

The measured absorption spectrum for a  $\text{BaTiO}_3$ :9%  $\text{Er}^{3+}$ /1%  $\text{Yb}^{3+}$  sample is shown in Fig. 5. The areas below the peaks have been obtained from this spectrum by numerical integration after correction for the baseline. In the 400–1600 nm range, the refraction index for the  $\text{BaTiO}_3$  host<sup>37</sup> can be satisfactorily described by Cauchy's equation

$$n = B + \frac{C}{\lambda^2} \quad (8)$$

with  $B = 2.24$  and  $C = 67\ 123.4\ \text{nm}^2$  yielding values between 2.66 and 2.27 for wavelengths in the range from 400 to 1600 nm. The measured lifetime for the  $^4\text{I}_{13/2}$  level is found to be  $\tau_{\text{exp}} = 4.61\ \text{ms}$ , and the corresponding spontaneous emission probability  $A_T = 216.9\ \text{s}^{-1}$ .

According to Carnall *et al.*<sup>36</sup> the magnetic dipole contribution to the oscillator strength for the  $^4\text{I}_{15/2} \rightarrow ^4\text{I}_{13/2}$  transition is given by  $f_{\text{md}} = n \times 30.82$ . Since at the wavelength for this

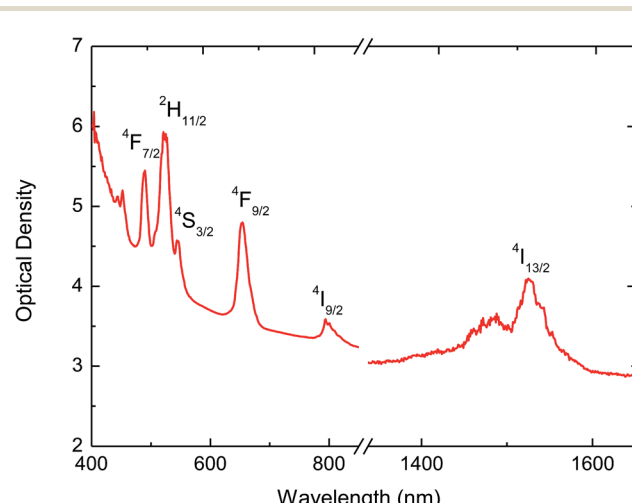


Fig. 5 Absorption spectrum for  $\text{BaTiO}_3$ : $\text{Er}^{3+}$  9%– $\text{Yb}^{3+}$  1% sample.



transition the refractive index of pure  $\text{BaTiO}_3$  is 2.26, we can estimate an oscillator strength due to magnetic dipole  $f_{\text{md}} = 70 \times 10^{-8}$  for our sample. Using eqn (9)

$$f(J \rightarrow J') = \frac{mc\lambda_m^2}{8\pi^2 e^2 n^2} \frac{(2J' + 1)}{(2J + 1)} A(J' \rightarrow J) \quad (9)$$

with  $J = 15/2$  and  $J' = 13/2$  and the experimental value  $A_T = 216.9 \text{ s}^{-1}$  for the total spontaneous emission probability we get a total oscillator strength  $f_{\text{exp}} = 134 \times 10^{-8}$ . By subtracting the magnetic dipole contribution from this value we finally arrive to  $f_{\text{ed}} = 64 \times 10^{-8}$  for the electric dipole contribution. These values have been used to calibrate the relative experimental  $\text{Er}^{3+}$  line strengths obtained from the spectrum by numerical integration of the areas below the different peaks. The calibrated values are given in the  $f_{\text{exp}}$  column in Table 2.

Judd-Ofelt intensity parameters  $\Omega_\lambda$  ( $\lambda = 2, 4, 6$ ) can be extracted from the experimental data by fitting the  $f_{\text{exp}}$  values in Table 2 to a set of  $f_{\text{calc}}$  values obtained from eqn (2) using the RELIC program.<sup>31</sup> For this purpose, we have used the crystal field and spin-orbit coupling parameters for  $\text{Er}^{3+}$  in aqueous solution given by Carnall in ref. 35:  $F_{(2)} = 440.8$ ,  $F_{(4)} = 66.8$ ,  $F_{(6)} = 7.3$ , and  $\zeta = 2380$ , all in units of  $\text{cm}^{-1}$ . The resulting JO intensity parameters are  $\Omega_2 = 1.3 \times 10^{-20}$ ,  $\Omega_4 = 0.9 \times 10^{-20}$ , and  $\Omega_6 = 0.4 \times 10^{-20} \text{ cm}^2$ . Using these parameters and eqn (2) we can estimate the oscillator strengths,  $f_{\text{calc}}$ , given in Table 2. The associated absolute RMS value is  $3.6 \times 10^{-7}$ .

The  $\Omega_\lambda$  parameters found for  $\text{Er}^{3+}$  in  $\text{BaTiO}_3$ :9%  $\text{Er}^{3+}$ /1%  $\text{Yb}^{3+}$  are in the range found for  $\text{Er}^{3+}$  in other mixed crystalline oxides.<sup>29</sup> Since the intensity of f-f transitions arises from the admixture of odd-parity crystal-field components their JO intensity parameters should depend on the type and symmetry of the ligands in a given material, although as noted by Hehlen *et al.*<sup>31</sup> it is difficult to establish clear correlations because the influence of the coordinating environment on the well-shielded 4f electrons is quite small. Besides this, comparison of  $\Omega_\lambda$  values reported in the literature is also hindered by the use of different procedures in their calculation, such as fitting the intensity parameters using optimized wavefunctions for the given material *vs.* using tabulated data obtained for another material, the types of transitions included in the fit, and the numerical details used in the fitting procedure. An additional difficulty in

**Table 2** Experimental and calculated emission intensities for  $\text{Er}^{3+}$  f-f transitions in  $\text{BaTiO}_3$ :9%  $\text{Er}^{3+}$ /1%  $\text{Yb}^{3+}$ . All transitions are from the ground state ( $^4\text{I}_{15/2}$ ) to the levels indicated in the first column of the table

Level	$\lambda$ (nm)	$f_{\text{rel}}$ (%)	$f_{\text{exp}}$ ( $10^{-8}$ )	$f_{\text{calc}}$ ( $10^{-8}$ )
$^4\text{I}_{13/2}$	1524	11.2	$64 + 70^a$	$78 + 75^a$
$^4\text{I}_{9/2}$	794	2.7	32	36
$^4\text{F}_{9/2}$	653	18.3	218	194
$^4\text{S}_{3/2}$	545	6.5	78	27
$^2\text{H}_{11/2}$	521	39.9	475	472
$^4\text{F}_{7/2}$	488	15.9	189	139
$^4\text{F}_{5/2}$	452	4.3	51	33
$^4\text{F}_{3/2}$	444	1.1	14	19

<sup>a</sup> Magnetic dipole contribution.

correlating JO parameters with structural features arises from the additivity of JO  $\Omega_\lambda$  values<sup>29</sup> since in the presence of several non-equivalent sites in the host matrix one obtains an average value for each  $\Omega_\lambda$  parameter. In general,  $\Omega_2$  has been found to scale with the degree of covalency between the rare earth cation and the coordinating ligands.<sup>29,31,38</sup> The small value found here is in concordance with those found for oxides with a strong ionic character. The  $\Omega_4$  and  $\Omega_6$  parameters have been found to decrease with increasing rigidity of the matrix.<sup>39</sup> According to this trend, the small values found here would be associated with the high rigidity of  $\text{BaTiO}_3$ , similar to that of other mixed crystalline oxides.

The calculated line strengths  $f_{\text{calc}}$  obtained from the fitted JO intensity parameters have been used to calculate spontaneous emission probabilities *via* eqn (7). The most relevant results are summarized in Table 3 where radiative lifetimes

$$\tau_{\text{rad}}^{-1} = \sum_J A(J' \rightarrow J) \quad (10)$$

and branching ratios

$$\beta_{J' \rightarrow J} = \tau_{\text{rad}} A(J' \rightarrow J) \quad (11)$$

have also been included.

### 3.5. Upconversion emission

UC spectra of the co-doped samples with different concentrations of  $\text{Er}^{3+}$  and  $\text{Yb}^{3+}$  are shown in Fig. 6. All spectra were obtained by exciting at 1500 nm. The emission spectra of  $\text{BaTiO}_3$ : $\text{Er}^{3+}$ - $\text{Yb}^{3+}$  phosphors show emission bands at 975 nm

**Table 3** Spontaneous emission probabilities, radiative lifetimes, and branching ratios calculated for  $\text{Er}^{3+}$  in  $\text{BaTiO}_3$ :9%  $\text{Er}^{3+}$ /1%  $\text{Yb}^{3+}$  using the JO intensity parameters  $\Omega_2 = 1.3 \times 10^{-20}$ ,  $\Omega_4 = 0.9 \times 10^{-20}$ , and  $\Omega_6 = 0.4 \times 10^{-20} \text{ cm}^2$

Transition	$\lambda$ (nm)	$A_{\text{ed}}$ ( $\text{s}^{-1}$ )	$A_{\text{md}}$ ( $\text{s}^{-1}$ )	$\tau_{\text{rad}}$ ( $\mu\text{s}$ )	$\beta_{J' \rightarrow J}$ (%)
$^4\text{I}_{13/2} \rightarrow ^4\text{I}_{15/2}$	1537	107	117	3898	100
$^4\text{I}_{11/2} \rightarrow ^4\text{I}_{13/2}$	2754	28	32	4115	25
$^4\text{I}_{15/2}$	975	183	—	—	75
$^4\text{I}_{9/2} \rightarrow ^4\text{I}_{11/2}$	4545	2	4	2498	1
$^4\text{I}_{13/2}$	1715	61	—	—	15
$^4\text{I}_{15/2}$	811	334	—	—	84
$^4\text{I}_{9/2} \rightarrow ^4\text{I}_{9/2}$	3387	5	12	318	1
$^4\text{I}_{11/2}$	1940	90	24	—	4
$^4\text{I}_{13/2}$	1138	150	—	—	5
$^4\text{I}_{15/2}$	660	2859	—	—	90
$^4\text{S}_{3/2} \rightarrow ^4\text{F}_{9/2}$	3052	1	—	430	0
$^4\text{I}_{9/2}$	1605	117	—	—	5
$^4\text{I}_{11/2}$	1186	54	—	—	2
$^4\text{I}_{13/2}$	829	642	—	—	28
$^4\text{I}_{15/2}$	538	1510	—	—	65
$^2\text{H}_{11/2} \rightarrow ^4\text{S}_{3/2}$	12 755	0	0	91	0
$^4\text{F}_{9/2}$	2463	33	1	—	0
$^4\text{I}_{9/2}$	1426	141	11	—	1
$^4\text{I}_{11/2}$	1085	142	806	—	9
$^4\text{I}_{13/2}$	779	212	257	—	4
$^4\text{I}_{15/2}$	517	9366	0	—	86



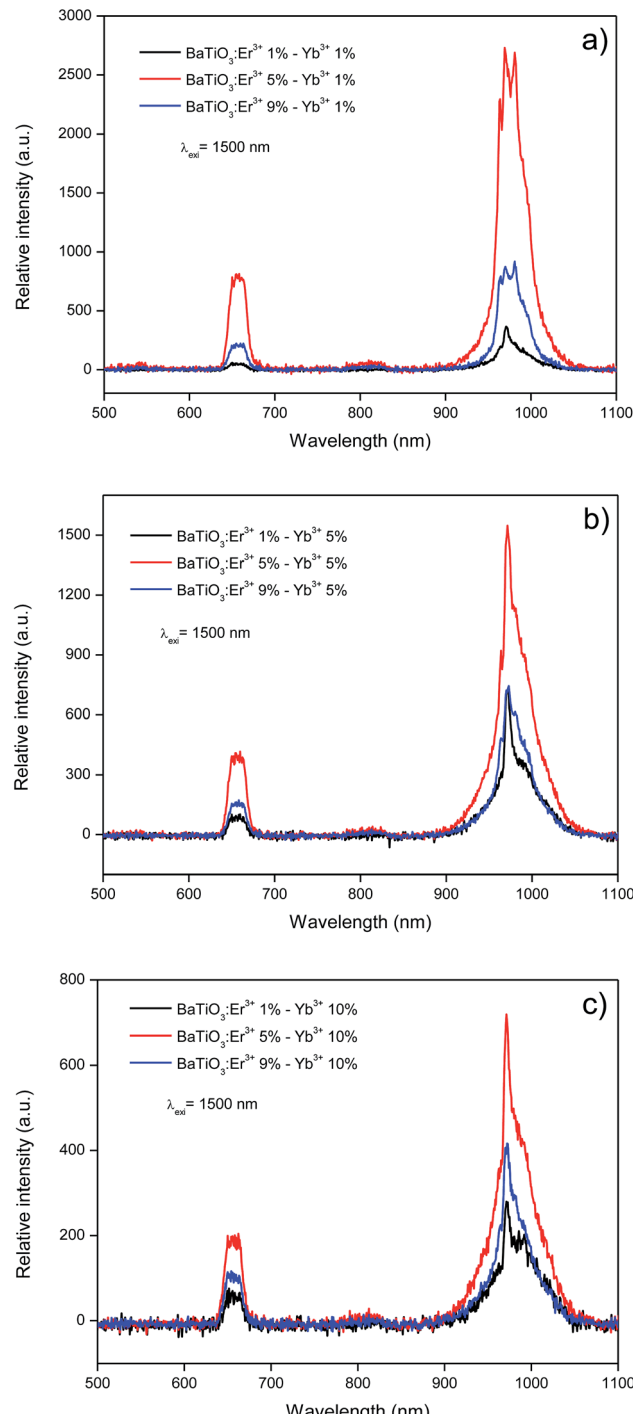


Fig. 6 Up-conversion spectra (excitation at 1500 nm) for  $\text{BaTiO}_3$ -based phosphors as a function of  $\text{Er}^{3+}$  and  $\text{Yb}^{3+}$  contents.

and 660 nm, which correspond to the electronic  ${}^4\text{I}_{11/2} \rightarrow {}^4\text{I}_{15/2}$  and  ${}^4\text{F}_{9/2} \rightarrow {}^4\text{I}_{15/2}$  transitions of the  $\text{Er}^{3+}$  ion, respectively. Moreover, at 975 nm the  ${}^2\text{F}_{5/2} \rightarrow {}^2\text{F}_{7/2}$  transition corresponding to  $\text{Yb}^{3+}$  ions is also present.

Comparing the intensity of the 975 nm band in the emission spectra for samples with different rare earth ion content (Fig. 7) it can be seen that in all cases, the sample doped with  $\text{Er}^{3+}$  at 5% that presents a maximal emission, being  $\text{BaTiO}_3:\text{Er}^{3+}$  5%– $\text{Yb}^{3+}$

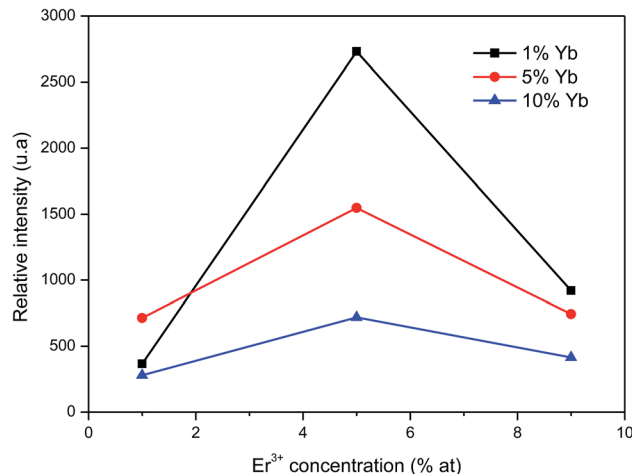


Fig. 7 Relative intensity of up-conversion emission as a function of  $\text{Er}^{3+}$  and  $\text{Yb}^{3+}$  ion concentrations using  $\lambda_{\text{exc.}} = 1500 \text{ nm}$ .

1% the composition yielding the highest photon UC (Fig. 6a). It is also observed that as the concentration of  $\text{Yb}^{3+}$  ion increases, the emission intensity decreases. This observation can be explained considering an increase of energy transfer and non-radiative processes that compete with luminescence as the concentration of sensitizer  $\text{Yb}^{3+}$  ions is increased.

As it is clearly visible in Fig. 6, the most intense emission corresponds to the 975 nm band, which corresponds precisely to the most interesting emission for applications in solar cells since it corresponds to the absorption band of silicon. Inclusion of  $\text{BaTiO}_3:\text{Er}^{3+}$ – $\text{Yb}^{3+}$  phosphors in these cells could then contribute to increase their photocurrent by harvesting also photons with a wavelength of 1500 nm.

To study the mechanism behind photon UC in  $\text{BaTiO}_3:\text{Er}^{3+}$ – $\text{Yb}^{3+}$  we have also studied the dependence of the intensity for the emissions at 975 and 660 nm as a function of the pump power of the incident laser. It is well-known that the upconversion intensity is directly related to the intensity of the infrared excitation by the following expression:

$$I_{\text{UC}} \propto I_{\text{IR}}^n \quad (12)$$

where  $n$  is the number of photons involved in the upconversion process.<sup>40,41</sup> In Fig. 8, the dependence of the logarithm of UC emission intensities for the 975 and 660 nm bands versus logarithm of the pumping power of the laser are shown. Fitting of the logarithmic curves according to eqn (12) the slopes,  $n$ , obtained for the  $\text{BaTiO}_3:\text{Er}^{3+}$  5%– $\text{Yb}^{3+}$  1% sample were 1.8 for the IR emission and 2.3 for the red one, indicating that the number of required photons in each case is 2 and 3, respectively.

The discrepancy between the actual values of the slope (1.8 and 2.3) and the number of photons involved in the process (2 and 3) is due to the known effect that the slope of the curve is gradually decreasing as the laser power increases, a phenomenon described by Pollnau *et al.*<sup>42</sup> as a saturation in the upconversion process at high power. According to this interpretation, a high pump power would increase the competition between the linear

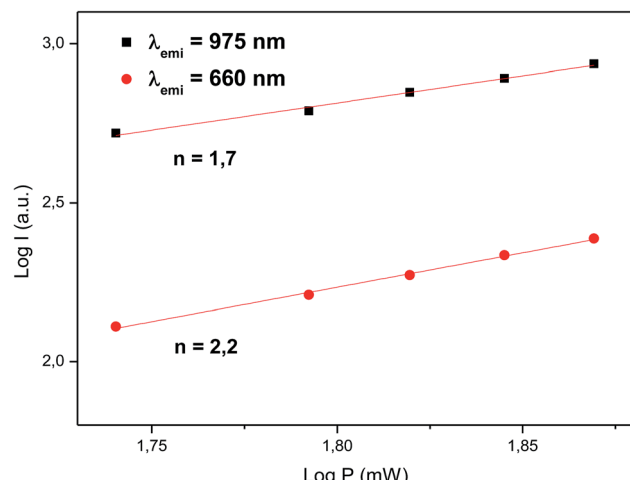


Fig. 8 Logarithm of the up-conversion emission intensity (excitation at 1500 nm) as a function of the logarithmic pump power of the excitation source.

decay and upconversion for the depletion of the intermediate excited states, resulting in a significantly reduced slope.

The dynamics of the 975 nm emission was studied by measuring the corresponding decay curves. Fig. 9 shows the decay curves for excitation at 1500 and 800 nm. In both cases, a rapid rise time is observed after excitation with the laser, followed by a rapid decline. This behavior is indicative of a GSA/ESA mechanism for the UC process in which after excitation by a pulsed laser at 1500 nm, the  $\text{Er}^{3+}$  ion is immediately excited to the  ${}^4\text{I}_{13/2}$  level by absorbing a photon and afterwards to the  ${}^4\text{I}_{9/2}$  level by absorbing a second 1500 nm photon. In this process, the population of the  ${}^4\text{I}_{9/2}$  level increases rapidly as a result of successive two-photon absorption, similar to what would be observed if this level is excited directly. Therefore, as it can be seen in Fig. 9, there is an immediate rise time after pulse excitation at 1500 nm, confirming the proposed upconversion mechanism. Subsequently a non-radiative relaxation to the  ${}^4\text{I}_{11/2}$  level takes place, from where the emission of a photon of wavelength 975 nm leads to the fundamental  ${}^4\text{I}_{15/2}$  state. In the same way, absorption of a third photon contributes to an increase in the population of the  ${}^4\text{S}_{3/2}$  level. Due to the small energy gap,  $\text{Er}^{3+}$  ions in the  ${}^4\text{S}_{3/2}$  state relax very quickly through a non-radiative process to the  ${}^4\text{F}_{9/2}$  levels from where they relax radiatively to the  ${}^4\text{I}_{15/2}$  ground state emitting a red photon (660 nm). Moreover, from the  ${}^4\text{I}_{11/2}$  level of the  $\text{Er}^{3+}$  ions,  $\text{Yb}^{3+}$  ions may be excited by resonant energy transfer processes. As observed in Fig. 10, the emission band by exciting at 800 nm of co-doped  $\text{BaTiO}_3:\text{Er}^{3+}-\text{Yb}^{3+}$  is broader than the emission band of doped  $\text{BaTiO}_3:\text{Er}^{3+}$ . It is due to the presence of the  $\text{Er}^{3+}:{}^4\text{I}_{11/2} \rightarrow {}^4\text{I}_{15/2}$  and  $\text{Yb}^{3+}:{}^2\text{F}_{5/2} \rightarrow {}^4\text{F}_{7/2}$  transitions in the codoped sample, confirming the energy transfer from the  $\text{Er}^{3+}$  to the  $\text{Yb}^{3+}$  ions.

As can be seen in Fig. 6, the UC emission intensity decreases with increasing  $\text{Yb}^{3+}$  ion concentration. A possible explanation for this result is the excitation of  $\text{Yb}^{3+}$  ions from  ${}^4\text{I}_{11/2}$  level of  $\text{Er}^{3+}$  (see Fig. 10) followed by a final transfer to traps in the matrix.<sup>43</sup>

The complete diagram for the proposed photon UC mechanism is shown in Fig. 11.

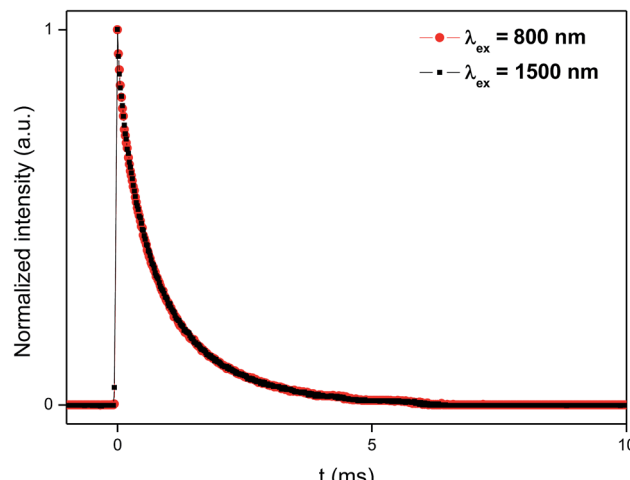


Fig. 9 Temporal evolution of the UC emission at 980 nm under pulse excitation at 1500 and 800 nm.

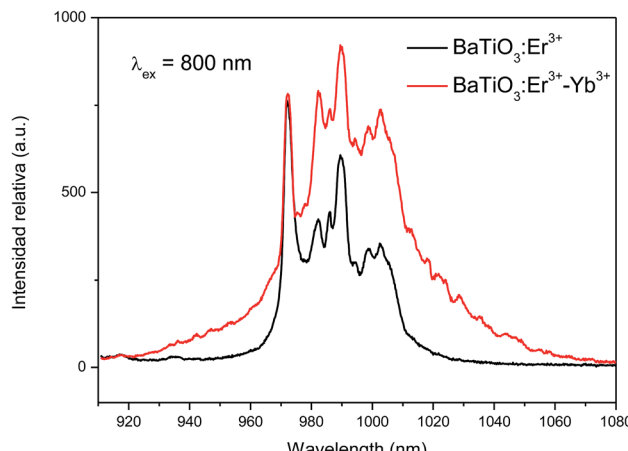


Fig. 10 Emission spectra for  $\text{BaTiO}_3:\text{Er}^{3+}$  5% and  $\text{BaTiO}_3:\text{Er}^{3+}$  5%– $\text{Yb}^{3+}$  1% exciting at 800 nm.

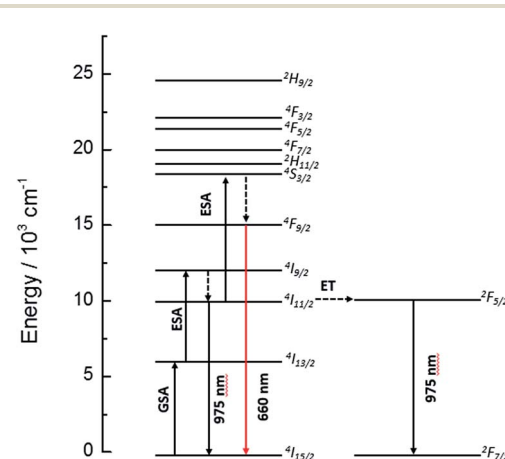


Fig. 11 Energy level diagram for the  $\text{Er}^{3+}$  and  $\text{Yb}^{3+}$  ions, indicating the suggested upconversion mechanisms taking place upon 1500 nm laser excitation.



## 4. Conclusions

$\text{Er}^{3+}/\text{Yb}^{3+}$  doped  $\text{BaTiO}_3$  phosphors were synthesized through a sol-gel method and their photon upconversion behavior was studied by excitation at 1500 nm. The results of PXRD measures show the existence of solid solutions for all phases in which the  $\text{Er}^{3+}$  and  $\text{Yb}^{3+}$  cations replace both the  $\text{Ba}^{2+}$  and  $\text{Ti}^{4+}$  sites. Raman spectroscopy corroborates the coexistence of the cubic and the tetragonal phases.

Our analysis of the optical properties of the new phosphors shows that their upconversion emission spectra are dominated by the emission at 975 nm ( ${}^4\text{I}_{11/2} \rightarrow {}^4\text{I}_{15/2}$ ), which has a potential use to increase the efficiency of Si solar cells by reducing transmission losses. The best UC behavior was observed for samples with a  $\text{BaTiO}_3:\text{Er}^{3+}$  5%– $\text{Yb}^{3+}$  1% composition. A detailed analysis shows that the emission at 975 nm is the result of a successive two-photon absorption of 1500 nm radiation. Finally, the decay curves of the emission at 975 nm by exciting at 1500 nm and 800 nm are in good agreement with a GSA/ESA mechanism for photon upconversion in these materials.

## Acknowledgements

The authors acknowledge Conicyt-Chile for the financial support (Anillo Grant ACT 1204). J. Ll, I. R. M. and P. A. acknowledge Fondecyt (Grant 1130248) for the international cooperation as well as MINECO and EU-FEDER (projects MAT2013-46649-C4-4-P, MAT2015-71070-REDC, MAT2016-75586-C4-4-P and CTQ2015-64579-C3-3-P). M. V. acknowledges CONICYT for a doctoral fellowship.

## References

- 1 B. S. Richards, *Sol. Energy Mater. Sol. Cells*, 2006, **90**, 2329.
- 2 M. A. Green, *Phys. E*, 2002, **14**, 65.
- 3 B. M. van der Ende, L. Aarts and A. Meijerink, *Phys. Chem. Chem. Phys.*, 2009, **11**, 11081.
- 4 W. G. J. H. M. van Sark, J. de Wild, J. K. Rath, A. Meijerink and R. E. I. Schropp, *Nanoscale Res. Lett.*, 2013, **8**, 81.
- 5 X. Huang, S. Han, W. Huang and X. Liu, *Chem. Soc. Rev.*, 2013, **42**, 173.
- 6 P. Ramasamy, P. Manivasakan and J. Kim, *RSC Adv.*, 2014, **4**, 34873.
- 7 C. Strümpel, M. McCann, G. Beaucarne, V. Arkhipov, A. Slaoui, V. Svtcek, C. del Cañizo and I. Tobias, *Sol. Energy Mater. Sol. Cells*, 2007, **91**, 238.
- 8 F. Auzel, *Chem. Rev.*, 2004, **104**, 139–173.
- 9 A. Shalav, B. S. Richards and M. A. Green, *Sol. Energy Mater. Sol. Cells*, 2007, **91**, 829.
- 10 H. Lian, Z. Hou, M. Shang, D. Geng, Y. Zhang and J. Lin, *Energy*, 2013, **57**, 270.
- 11 W. Yang, X. Li, D. Chi, H. Zhang and X. Liu, *Nanotechnology*, 2014, **25**, 482001.
- 12 F. Wang and X. Liu, *Chem. Soc. Rev.*, 2009, **38**, 976.
- 13 H.-Q. Wang, M. Batentschuk, A. Osset, L. Pinna and C. J. Brabec, *Adv. Mater.*, 2011, **23**, 2675.
- 14 D. R. Gamelin and H. Güdel, *Top. Curr. Chem.*, 2001, **214**, 1.
- 15 D. P. Dutta, A. Ballal, J. Nuwad and A. K. Tyagi, *J. Lumin.*, 2014, **148**, 230.
- 16 S. Fuentes, N. Barraza, E. Veloso, R. Villarreal and J. Llanos, *J. Alloys Compd.*, 2013, **569**, 52.
- 17 J. Long, L. Yang and X. Wei, *J. Alloys Compd.*, 2013, **549**, 336.
- 18 Y. Tsur, T. D. Dunbar and C. A. Randall, *J. Electroceram.*, 2001, **7**, 25.
- 19 S. D. Shannon, *Acta Crystallogr., Sect. A: Cryst. Phys., Theor. Gen. Crystallogr.*, 1976, **32**, 751.
- 20 U. D. Venkateswaran, V. M. Naik and R. Naik, *Phys. Rev. B: Condens. Matter Mater. Phys.*, 1998, **58**, 14256.
- 21 Z. Yao, H. Liu, Y. Liu, Z. Wu, Z. Shen, Y. Liu and M. Cao, *Mater. Chem. Phys.*, 2008, **109**, 475.
- 22 A. Garrido-Hernández, A. García-Murillo, F. d. J. Carrillo-Romo, L. A. Cruz-Santiago, G. Chadeyron, A. d. J. Morales-Ramírez and S. Velumani, *J. Rare Earths*, 2014, **32**, 1016.
- 23 P. Hermet, M. Veithen and P. Ghosez, *J. Phys.: Condens. Matter*, 2009, **21**, 215901.
- 24 E. Chávez, S. Fuentes, R. A. Zárate and L. Padilla-Campos, *J. Mol. Struct.*, 2010, **984**, 131.
- 25 H. Hayashi, T. Nakamura and T. Ebina, *J. Phys. Chem. Solids*, 2013, **74**, 957.
- 26 D. Caruntu, T. Rostamzadeh, T. Costanzo, S. S. Parizi and G. Caruntu, *Nanoscale*, 2015, **7**, 12955.
- 27 B. R. Judd, *Phys. Rev.*, 1962, **127**, 750.
- 28 G. S. Ofelt, *J. Chem. Phys.*, 1962, **37**, 511.
- 29 C. Görller-Walrand and K. Binnemans, Spectral intensities of f-f transitions, in *Handbook on the Physics and Chemistry of Rare Earths*, ed. K. A. Gschneidner Jr and L. Eyring, North-Holland, 1998, vol. 25, p. 101.
- 30 B. M. Walsh, Judd–Ofelt theory: principles and practices, in *Advances in Spectroscopy for Lasers and Sensing*, ed. B. Di Bartolo and O. Forte, Springer, Netherlands, 2006, p. 403.
- 31 M. P. Hehlen, M. G. Brik and K. W. Krämer, *J. Lumin.*, 2013, **136**, 221.
- 32 W. Luo, J. Liao, R. Li and X. Chen, *Phys. Chem. Chem. Phys.*, 2010, **12**, 3276.
- 33 G. Yao, C. Lin, Q. Meng, P. S. May and M. T. Berry, *J. Lumin.*, 2015, **160**, 276.
- 34 E. Cantelar, M. Marin-Dobrincic, T. Jardiel, A. C. Caballer and F. Cussó, *Opt. Mater.*, 2015, **41**, 122.
- 35 W. T. Carnall, P. R. Fields and K. Rajnak, *J. Chem. Phys.*, 1968, **49**, 4424.
- 36 W. T. Carnall, The absorption and fluorescence spectra of rare earth ions in solution, in *Handbook on the Physics and Chemistry of Rare Earths*, ed. K. A. Gschneidner Jr and L. Eyring, North Holland, 1979, vol. 3, p. 171.
- 37 S. M. Wemple, M. Didomenico and I. Camlibel, *J. Phys. Chem. Solids*, 1968, **29**, 1797.
- 38 D. E. Henrie, R. L. Fellows and G. R. Choppin, *Coord. Chem. Rev.*, 1976, **18**, 199.
- 39 C. K. Jorgensen and R. Reisfeld, *J. Less-Common Met.*, 1983, **93**, 107.



40 B. M. van der Ende, L. Aarts and A. Meijerink, *Phys. Chem. Chem. Phys.*, 2009, **11**, 11081.

41 W. Yu, Y. Tian, M. Xing, Y. Fu, H. Zhang and X. Luo, *Mater. Res. Bull.*, 2016, **80**, 223.

42 M. Pollnau, D. R. Gamelin, S. R. Lüthi, H. U. Güdel and M. P. Helen, *Phys. Rev. B: Condens. Matter Mater. Phys.*, 2000, **61**, 3337.

43 M. A. Hernández-Rodríguez, M. H. Imanieh, L. L. Martín and I. R. Martín, *Sol. Energy Mater. Sol. Cells*, 2013, **116**, 171.

